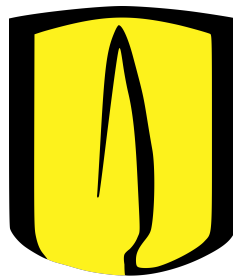


Observational evidence of star formation stochasticity in the CALIFA dataset

Nicolás Romero Díaz

201127499

Advisor: Jaime Forero-Romero



Contents

1	Introduction	2
2	Theoretical framework	4
2.1	Stochasticity in star formation	4
2.2	Measuring stochasticity	7
2.2.1	The Balmer decrement	7
2.2.2	The IMF	8
3	The CALIFA survey	10
3.1	The CALIFA survey	10
3.2	The CALIFA datacubes	11
3.3	The Pipe3D outputs	11
4	Data analysis	12
4.1	Analysis of the stellar population	12
4.2	Analysis of strong emission lines	13
5	Results	14
6	Discussion	23
6.1	The H_α/H_β ratio	23
6.2	The OII EW	24
7	Conclusions	26
7.1	Further work	27
8	Appendix	28
8.1	List of galaxies	29
8.2	Additional results	30

Chapter 1

Introduction

Star formation processes turn galactic gas clouds into stars. These processes are probabilistic by nature and can be parametrized by two components: the initial mass function (IMF) and the cluster mass function (CMF).

The IMF outlines the relative abundance of stars of a certain mass to be formed, and is represented by $\phi(m)$. For the most part, the relevant characteristics of the IMF are described by two pieces of information. (i) The mass interval, describing the available range of mass possible for the stars being generated ($m_{min} - m_{max}$); (ii) the relative abundance of stars with different stellar masses, taken as $\phi(m) \propto m^{-\gamma}$. When $\gamma > 0$ less massive stars are more likely to be formed. The second parameter arises from the fact that star formation is mainly a cluster phenomenon [1], characterized by the cluster mass function, $\psi(M_{ecl})$. This CMF describes the number of clusters in a region where stars are being produced, with M_{ecl} the cluster mass [2].

The sampling of both the IMF and CMF is influenced by the star formation rate (SFR) of a particular system. If the SFR is low in a given region the sampling of the IMF and CMF becomes more challenging. Authors in [3] have proposed that in these areas, stochastic processes have a greater influence over the statistical nature of both the IMF and CMF. This statistical foundation of the mass functions has several distinct effects that influence different spectral properties of gas clouds surrounding star forming localities. In particular, stochasticity appears to cause the ratio of H_α/H_β intensity to fluctuate around a mean value [3].

Using the public SLUG code (Stochastically Light Up Galaxies), Forero-Romero and Dijkstra [2] have found that this fluctuation around a mean value also takes place when comparing the ratio of Lyman alpha (Ly_α) flux to

the FUV photons. This relation is a well known spectral quantity called the equivalent width (EW), which characterizes the Ly_α emission line strength. The interest in the EW and its fluctuation arises from the fact that the Ly_α line is a powerful indicator of stellar populations and intergalactic dust and can be a determining factor for classification of galaxies [2]. In another work, Mas-Ribas et.al [4] also observed fluctuation of the Ly_α luminosity when performing stochastic IMF sampling.

The appearance of stochasticity and its effects on spectral properties is discussed in the theoretical framework presented in chapter two. A review of computational predictions as well as how spectral data can be affected by phenomena in the interstellar medium (i.e. galactic extinction) is also included in this chapter.

In order to search for this stochastic effects, we will use data published by the Calar Alto Legacy Integral Field Area Survey (CALIFA), reported in detail by Sánchez et. al. [5][6]. A compendious description of the CALIFA data will be presented in chapter three, as well as an overall description of the survey.

The minutiae of the handling of CALIFA data is detailed in chapter four, as well as a discussion of the different computational tools used to navigate this data. This chapter will also including a general outline of the Pipe3D analysis pipeline developed by the CALIFA team of Sánchez et. al. [7]

Representative results are included in chapter five.

In chapter six we present a discussion of the results obtained. The detection and quantification of stochasticity on our analysis is included. Finally, we present our conclusions in chapter seven, followed by a list consisting of all galaxies researched for this work in the appendix.

Chapter 2

Theoretical framework

2.1 Stochasticity in star formation

In a region where stars are being produced, these stars will ionize gas clouds adjacent to them. Less massive stars ionize gas clouds in lesser proportion than their more massive counterparts, making this gas emission spectra dimmer in comparison. In order to separate low SFR regions from higher SFR regions we analyze the H_α emission line intensity. This line is an indicator of SFR since it is produced by gas ionized by young, hot stars [8]. Greater H_α intensity corresponds to larger SFR and lower intensity to lesser SFR following the tendency represented in the following formula[9]:

$$\text{SFR}(\text{M}_\odot\text{yr}^{-1}) = 7.9 \times 10^{-42} L(H_\alpha)(\text{ergs s}^{-1}) \quad (2.1)$$

with $L(H_\alpha)$ the luminosity of the emission line. The SFR is given in units of solar masses per year ($\text{M}_\odot\text{yr}^{-1}$).

In simulations presented in [2], [3] stochastic effects causes the value of different line intensity ratios to fluctuate, with regions of low SFR being most affected. We can illustrate star formation stochasticity with an example: a weighted die that is more likely to cast a lower number. If the die is thrown many times then we will have a good sampling of the probability distribution. On the contrary, if the die is thrown only a few times, the probability distribution will not be sampled accurately.

In this analogy the lower numbers are the less massive stars and the die that is thrown many times is a region of high SFR. When a star forming locality has a high SFR, sampling the IMF is straightforward. If a region presents a low SFR the probability of finding massive stars decreases [3] and thus the IMF is not completely sampled. Since the relation of stellar

luminosity and stellar mass is highly nonlinear[10], having an IMF that is not completely sampled makes the sequence in which stars fill a particular population's mass very significant in terms of luminosity output. In this case, the relation between the total mass and the luminosity of a stellar population is no longer deterministic [11]

There is also finite sampling in time since some evolutionary stellar phases of massive stars are brief. This is significant since the ionization luminosity in different phases has important variations [3].

Furthermore, the fact that most stars are formed in clusters gives rise to two additional effects: (i) the maximum stellar mass can not be greater than the cluster mass M_{ecl} , and (ii) at low SFR, a star forming region is not producing stars at a constant rate, instead, its output consists of a series of star formation bursts, with each burst corresponding to the formation of a new stellar cluster [3].

The finite samplings in both mass and time, conditions upon maximum mass and the irregular bursts of star formation at low SFRs are the motivation for searching for stochasticity in these low SFR regions.

In [3], Forero-Romero et. al. found that when stochastic effects are taken into consideration the measured EW varied from $\sim EW_0/4$ to $\sim 3 \times EW_0$, with EW_0 the expected value for the EW. The authors describe the behavior of this effect as a SFR dependent probability density function (PDF) at a given SFR as a double power law of the form:

$$P(\mathcal{M}|\text{SFR}) = P_0 \left[\left(\frac{\mathcal{M}}{\mathcal{M}_0} \right)^{-\alpha} + \left(\frac{\mathcal{M}}{\mathcal{M}_0} \right)^{\gamma} \right]^{-1} \quad (2.2)$$

with \mathcal{M} a dimensionless parameter defined as:

$$\mathcal{M} \equiv \frac{EW}{EW_0} \quad (2.3)$$

In the same work, the authors assume that the totality of star formation happens in clusters ($f_c = 1$). This reduces the fluctuation of the emission line flux by approximately an order of magnitude [12]. The authors obtain this answer considering a range of stellar masses from $0.08M_\odot$ to $120M_\odot$ and a cluster mass interval spanning values of $20\text{--}10^7M_\odot$, assuming a Salpeter IMF. The final section of this chapter is dedicated to the relevance of the choice of IMF, as well as the presentation of some generalities.

The star formation rate is present by the constants $P_0, \mathcal{M}_0, \alpha, \gamma$. This double power law is valid for values of $P(\mathcal{M}|\text{SFR}) > 10^{-2}$ due to the limited number of points available to perform a thorough fit of the data. This PDF

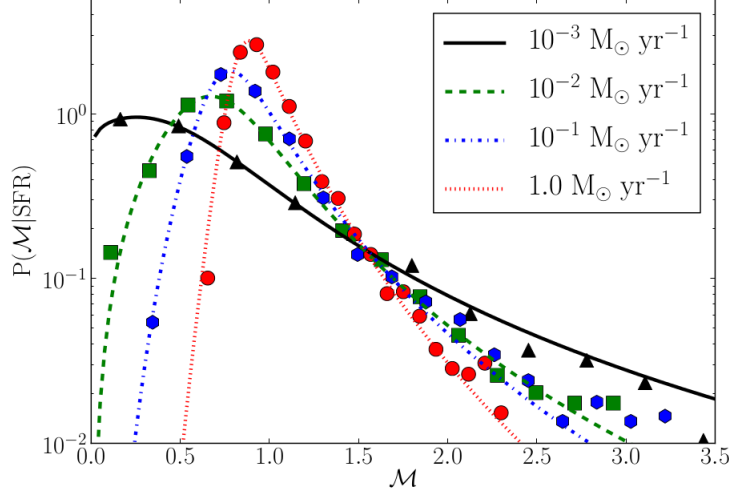


Figure 2.1: Visualization of equation 2.2 for different SFR. Taken from [2]

is visualized in figure 2.1 for multiple star formation rates. In this figure, it is clear that as SFR increases, the peak of the function becomes more pronounced. Ideally, if no external effects are present, this plot would consist of a delta function centered around $\mathcal{M} = 1$ [2].

In a separate work, Mas-Ribas et. al. [4] also found fluctuation of the Ly_α line intensity when performing stochastic IMF sampling. In absence of stochasticity, these theoretical results shown in figure 2.2 should consist of a thin line along the expected Ly_α luminosity [4]. The column on the left has lower SFR, the middle column has a higher SFR and the column on the right has the highest SFR. Therefore, when stochasticity is present in simulations we see a distribution of values of Ly_α luminosity around a mean value, once again with regions of low SFR being the most sensitive to stochasticity. The same effects can be seen in the $HeII\lambda 1640$ line. This simulations were performed making a stochastic sampling of the IMF and taking periods of star formation bursts of $1000M_\odot$ per Myr [4].

As we can see, stochastic effects in simulations cause fluctuation of multiple spectral parameters, including the Ly_α EW and luminosity and the H_α/H_β ratio. In this work, we look at the emission spectra of gas clouds and study the H_α/H_β ratio for fluctuations around a mean value as found in simulations by [3].

Expanding on conclusions from [3] a study of the EW of the OII line is also presented. According to their theoretical results, stochasticity should

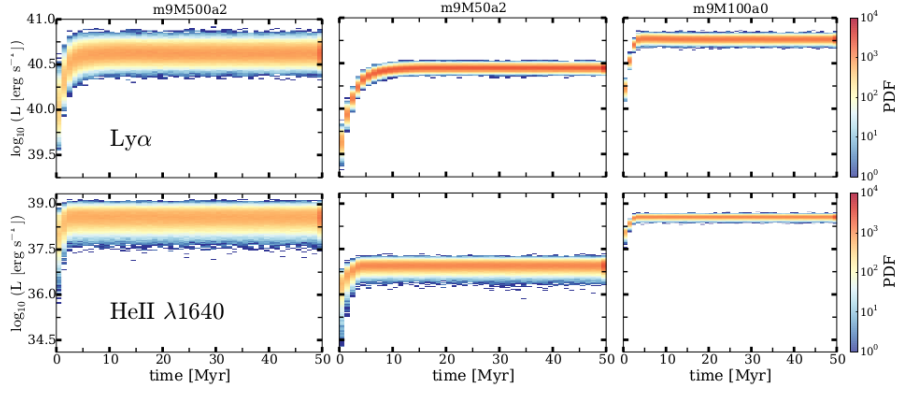


Figure 2.2: Fluctuation of the $Ly\alpha$ and $HeII\lambda 1640$ luminosity for a stochastically sampled IMF.

produce a similar distribution in other emission lines. This means that performing our analysis and comparing the values of OII EW in regions of low SFR with values in regions of SFR should yield analogous results.

2.2 Measuring stochasticity

When measuring stochasticity it is important to take galactic extinction into account. Since the predicted effects of stochasticity is the fluctuation of spectral parameters, any effects that influence observational data must be studied and quantified.

Results obtained in the field of stellar astrophysics are fundamentally affected by the selection of the IMF. The IMF is an empirical formula that illustrates the probability with which a star of a certain mass is found. Since stars of different masses ionize surrounding gas clouds in varying degrees, we must observe the choice of IMF when making an interpretation of our results.

In this section the phenomenon of galactic extinction, also known as either the Balmer decrement or interstellar reddening, is detailed. A breakdown of the two most widely used IMFs is also included.

2.2.1 The Balmer decrement

The Balmer decrement is a phenomenon that occurs when electromagnetic radiation passes through a dust cloud in the interstellar medium. These dust particles are micron sized, which causes a greater absorption of bluer

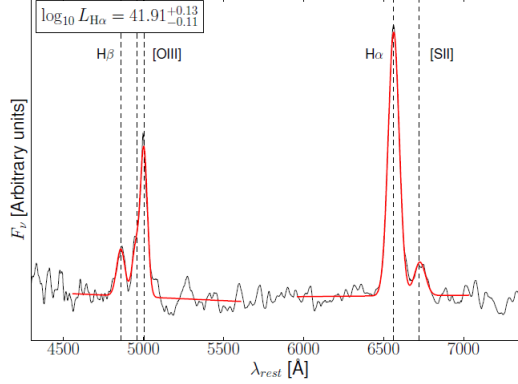


Figure 2.3: Difference in H_α and H_β intensities. Taken from [13]

light as it is more likely to collide with the particle. This means that when we observe this light it will appear redder.

When we analyze the H_α/H_β ratio this absorption must be taken into account, since the H_β emission line has a shorter wavelength than H_α and will more likely collide with dust particles and affect our measured value of H_α/H_β . This attenuation of H_β means that when checking for the value of H_α/H_β we will observe a greater number since H_β has become dimmer in comparison to H_α . The difference of intensities for these lines can be seen in figure 2.3 [13].

This effect means that not every variation of the observed spectra is caused solely by stochasticity. In fact, to properly quantify the presence of stochasticity, or lack thereof, we must isolate our data from any external effects presented by outside influence on the data used.

2.2.2 The IMF

The IMF of any stellar cluster is believed to be relatively invariant from one group of stars to the other [14]. This stellar parameter quantifies $N(m)dm$, the number of stars with masses between m and $m + dm$, represented commonly in literature as $\xi(m)\Delta m$. Even though it is an empirical function, there are two models that are relevant to this work, the Salpeter IMF[15] and the Kroupa IMF.

The Salpeter IMF is:

$$\xi(m\Delta m) = \xi_0 \left(\frac{m}{M_\odot} \right)^\alpha \left(\frac{\Delta m}{M_\odot} \right) \quad (2.4)$$

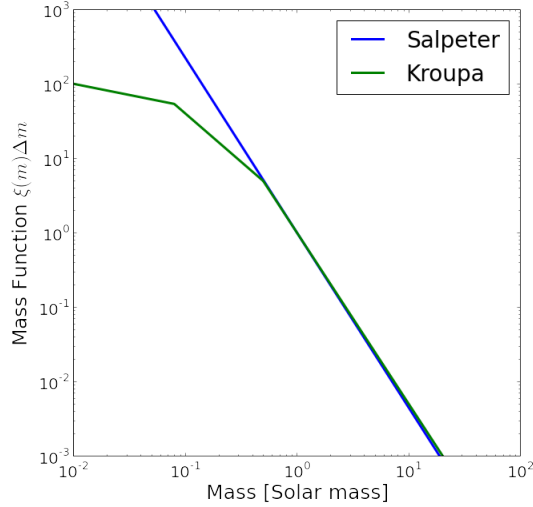


Figure 2.4: Visualization of the Salpeter IMF and Kroupa IMF

And the Kroupa IMF:

$$\xi(m) = m^{-\alpha} \quad (2.5)$$

The difference between both arising from the distribution of the more massive stars, since Salpeter takes the α parameter as independent of the stellar mass m with a value of $\alpha = -2.35$. On the other hand, Kroupa adjusts this parameter according to different ranges of stellar masses, maintaining $\alpha = 2.35$ $m > 2.3$; $\alpha = 1.3$, $0.08M_{\odot} < m < 0.5M_{\odot}$ and $\alpha = 0.3$; $m < 0.08M_{\odot}$. This causes the number of massive stars in the Kroupa IMF to be lower than the one predicted by the Salpeter IMF.

The differences of these IMFs can be seen in figure 2.4. We can observe the segmented Kroupa IMF curve corresponding to threshold values of the stellar mass. In the article that inspired this work, a Salpeter IMF is selected, while a Kroupa IMF used in [3] with which whom we will be going back and forth regularly in this work. Despite the different characterizations of stellar populations, results in [3] are not significantly influenced by the selection of the IMF.

Chapter 3

The CALIFA survey

In this chapter we present an overview of the CALIFA survey, including several generalities concerning the CALIFA datasets. In particular, we discuss the selection criteria of the galaxies relevant to this work. In addition, a brief description of the two different configurations available for CALIFA data is presented as well as some generalities of the output of the Pipe3D analysis pipeline.

3.1 The CALIFA survey

The CALIFA survey is a comprehensive wide field integral field unit (IFU) survey carried out in the Calar Alto observatory in Almería, Spain. It is operated jointly with the Max Planck Insitut für Astronomie and the Instituto de Astrofísica de Andalucía. Observations began in June of 2010, with the survey collecting data from over six hundred galaxies in two configurations, the V500 and the V1200 set ups [5] described in the following section.

The reasoning for selecting CALIFA survey data is simple. As seen in figure ??, CALIFA data does not consists of a single spectra, instead, multiple optic fibers were pointed at a single galaxy [5] [6]. For previous surveys having a single measure of a spectra meant that for an entire galaxy there was only one reported value of total SFR. Since stochasticity theoretically appears in low SFR regions, the ability to focus on distinct regions that have lower SFR opens the possibility of searching for this stochastic effects.

In this work, we will be using “face on” galaxies from the CALIFA catalog published in [7]. These type of galaxies are optimal for a complete scanning and allow us to measure the spectra of individual regions within a galaxy. We did a manual selection of the datacubes in [7] to select galaxies whose

galactic planes are perpendicular to our field of view.

3.2 The CALIFA datacubes

The CALIFA datacubes consist of a three dimensional array, where the x and y coordinates indicate the right ascension and declination of the target, and the z axis contains information about flux intensity and wavelength of that pixel along with the error associated with those fluxes, a mask to cover bad pixels and the covariance weight of the error propagation [5] [6].

The V500 and V1200 configurations cover different wavelength intervals and have different resolution, with the V500 datacube having a resolution of $\lambda/\Delta\lambda \sim 850$ and covering emission lines between $3745 - 7500 \text{ \AA}$, while the V1200 configuration has a higher resolution of $\lambda/\Delta\lambda \sim 1650$ and compiles wavelengths from $3700 - 4800 \text{ \AA}$. [5] [6]

In this work, we will be using the lower resolution V500 datacubes published in [7] which have been subjected to the Pipe3D analysis pipeline explained in section 3.2 and detailed in [7]. These datacubes contain a great deal of information, including that of intermediate steps of the fitting procedure.

3.3 The Pipe3D outputs

In the case of this study, we are interested in fluctuations of the EW of the OII line emitted by gas clouds that surround star forming regions. The OII EW is defined as the ratio between the intensity of the OII emission line and the continuum radiation in its vicinity. This means that we need a robust fitting procedure in order to characterize both this emission line spectra and continuum radiation since they will greatly affect our data of the EW.

The Pipe3D pipeline proposed by Sánchez et.al [7] consist of a series of steps followed in order to organize and successfully provide a fit for the spectra in the CALIFA datacubes. Since the original data consists of a superposition of spectra of gas clouds in interstellar environments as well as the underlying star population, these two spectra have to be treated using several procedures. It is also important to make a distinction between weak and strong emission lines since fitting procedures are different for each. Since we will be studying H_α , H_β and OII lines, we will not include the fitting procedure of weak emission lines.

Chapter 4

Data analysis

In this chapter, we discuss the details of the computational tools pertinent to this work. We will review the different libraries and procedures that have been applied in order to organize and analyze the different CALIFA datacubes. Specifically, we will discuss some the fitting procedures implemented by the CALIFA team [7] which are relevant to this work.

4.1 Analysis of the stellar population

By applying an algorithm known as “CS-binning algorithm”, the CALIFA team has produced a set of spectral data with which they are able to study the spectra of the stellar population. This algorithm consists of dividing the datacubes into two dimensional cells called “spatial bins” and subsequently taking the mean value of the pixels included, masking pixels with bad values. Once the averaged spectra is accounted for, the CALIFA team applied the Pipe3D analysis pipeline, which is able to fit the observed data via an iterative procedure [7]. When applying this procedure, there appears an associated error for these new binned spectra since bad pixel data can adversely modify the resultant dataproducit. Pipe3D provides the associated error of each spaxel as part of the original datacube. The ultimate goal of this analysis is to be able to obtain an optimum depiction of the stellar population and subtract it from the datacubes, leaving the remaining data of the spectra associated exclusively with the emission lines of the gas clouds in interstellar regions of the galaxy. The results obtained by CALIFA are public and presented in [7].

After this binning procedure, several maps are created:

- Row Stack Spectra (RSS)

- A position table for each galaxies binned cube, corresponding to the indices of the spatial bins from brightest to dimmest.
- Two intensity maps at the wavelength range of the V-band, with one map corresponding to the intensity before the binning procedure and the other one to the binned data.

Once this results were obtained, the stellar population was fitted with a Simple Stellar Population (SSP) template and thus the systemic velocity, the velocity dispersion and dust attenuation could be derived.

The final step consists of fitting the strong emission lines and subtracting them from the datacube obtained at this stage. Then, the procedure is repeated until a certain condition of χ^2 is met. The fitting of strong emission lines is presented in the following section. The results obtained by CALIFA are public and presented in [7].

4.2 Analysis of strong emission lines

A Gaussian fit, though not sophisticated, is valid for fitting strong emission lines. The CALIFA team divides the observed wavelengths into four groups:

- $[O]_{II}\lambda 3727$ (3700 – 3750) Å
- $H_\beta, [O_{III}]\lambda 4959$ and $[O_{III}]\lambda 5707$ (4800 – 5050) Å
- $[N_{II}]\lambda 6548, H_\alpha$ and $[N_{II}]\lambda 6583$ (6530 – 6630) Å
- $[S_{II}]\lambda 6717, [S_{II}]\lambda 6731$ (6680 – 6770) Å

since we will not be taking into account gas-rich major merger galaxies, AGN nuclei nor galaxies that intercept in our observational foreground, this gaussian fit is valid for our work.

Before assigning a gaussian function to a particular emission line, authors in [7] do a first guess of kinematic properties based on the expected H_α wavelength of the radiation. They take into account that particular galaxies redshift and by making a parabolic approximation to the centroid of the emission line.

Finally, the emission line is fitted by using a small range of systematic velocities centered around the initial guess. This procedure results in a set of maps of an *emission line pure cube* which includes different parameters for each emission line [7]. Once again, the results obtained by CALIFA are public and presented in [7].

Chapter 5

Results

For representative results of the analysis applied we will present four galaxies: (i) IC4566; (ii) NGC0001; (iii) NGC0036 (iv) UGC09476 in figures 5.1 to 5.4.

We begin by visualizing each galaxy's OII, H_α and H_β intensities. Then, we plot the H_α/H_β ratio that Fumagalli checked for stochasticity in [3]. Taking the logarithm in base ten gives us a clearer view of smaller variations in the values of this ratio. Since stochasticity would theoretically alter the values of this quotient, we will present the $\log H_\alpha$ vs. $\log H_\alpha/H_\beta$ distribution in more detail in figure 5.5. By visualizing the $\log H_\alpha$ values plotted against the $\log H_\alpha/H_\beta$ we can more easily identify regions of low SFR.

Making a histogram from the data in figure 5.5, we obtain figure 5.6. It is important to separate the H_α data in three regions. A bright region, a mid-range region and a faint region. By dividing the range of values that H_α spans on the horizontal axis of figure 5.5 in three equal parts we can distinguish these three regions. These three tiers are then classified by H_α intensity. The upper tier has the highest H_α values (i.e. the highest SFR), the middle tier has intermediate values and the lower tier has the lowest values. Thus, the bright region consist of the H_α/H_β data that lies on the upper tier of the values of H_α . The mid-range region is the H_α/H_β data that lies in the middle tier and the dim region is the one in which H_α/H_β values lie on the lowest tier of values of H_α .

The bright region is plotted in red, the mid-range spectra is green and the faint spectra in blue. The distinction arises from the fact that stochastic effects appear in simulations when there is low SFR and therefore have a dimmer spectra. The segmented vertical line indicates the theoretical value

for the H_α/H_β ratio, which is 2.85^1 and whose value is theoretically affected by stochasticity.

After plotting the data in figure 5.6 we perform a fit of this results and obtain a probability density function for values of H_α/H_β across all regions of the spectra. The resulting curves are plotted for our four representative galaxies (figure 5.7). Estimations of the free parameters obtained for several other galaxies are plotted one against the other to facilitate comparison. These free parameters are the ones present in equation 2.2, which are P_0 , \mathcal{M}_0 , α and γ . The full list of galaxies studied is included in the appendix as well as detailed results for other galaxies.

IC4566

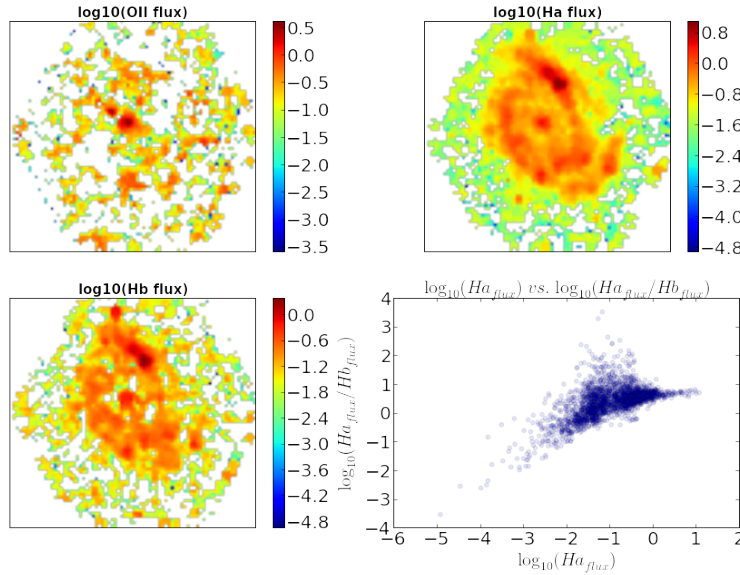


Figure 5.1: a) OII flux, b) H_α flux, c) H_β flux, d) $\log(H_\alpha)$ vs. $\log(H_\alpha/H_\beta)$

¹Osterbrock, Astrophysics of Planetary Nebulae and Active Galactic Nuclei, University Science Books, 1989

NGC0001

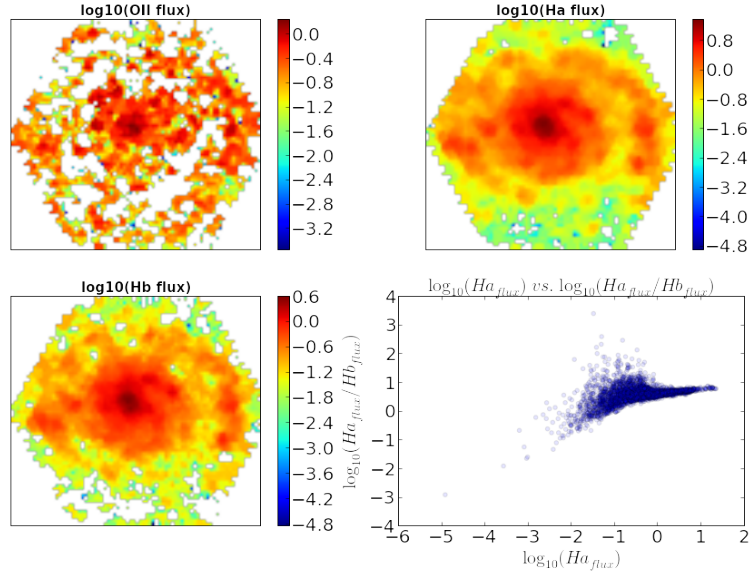


Figure 5.2: a) OII flux, b) H α flux, c) H β flux, d) $\log(\text{H}\alpha)$ vs. $\log(\text{H}\alpha/\text{H}\beta)$

NGC0036

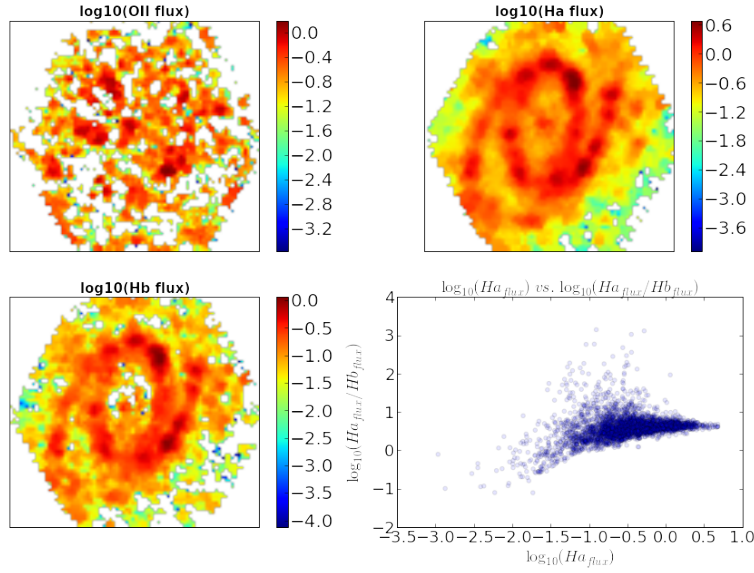


Figure 5.3: a) OII flux, b) H α flux, c) H β flux, d) $\log(\text{H}\alpha)$ vs. $\log(\text{H}\alpha/\text{H}\beta)$

UGC09476

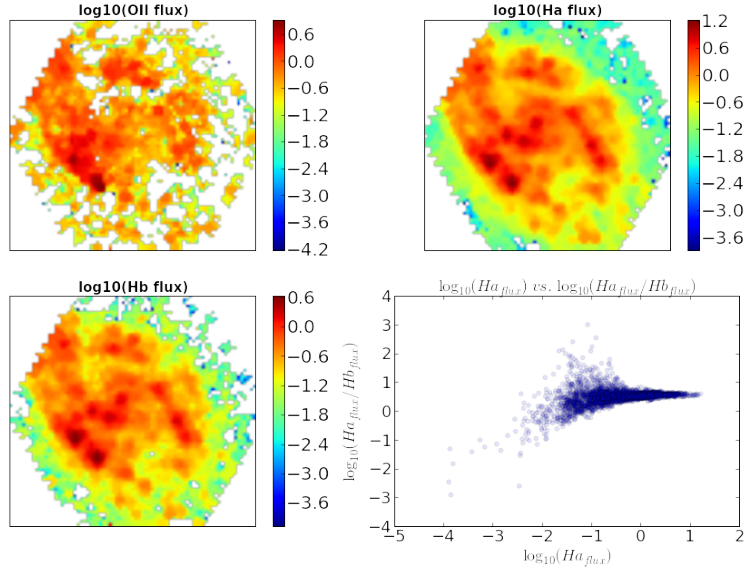


Figure 5.4: a) OII flux, b) H_{α} flux, c) H_{β} flux, d) $\log(\text{H}_{\alpha})$ vs. $\log(\text{H}_{\alpha}/\text{H}_{\beta})$

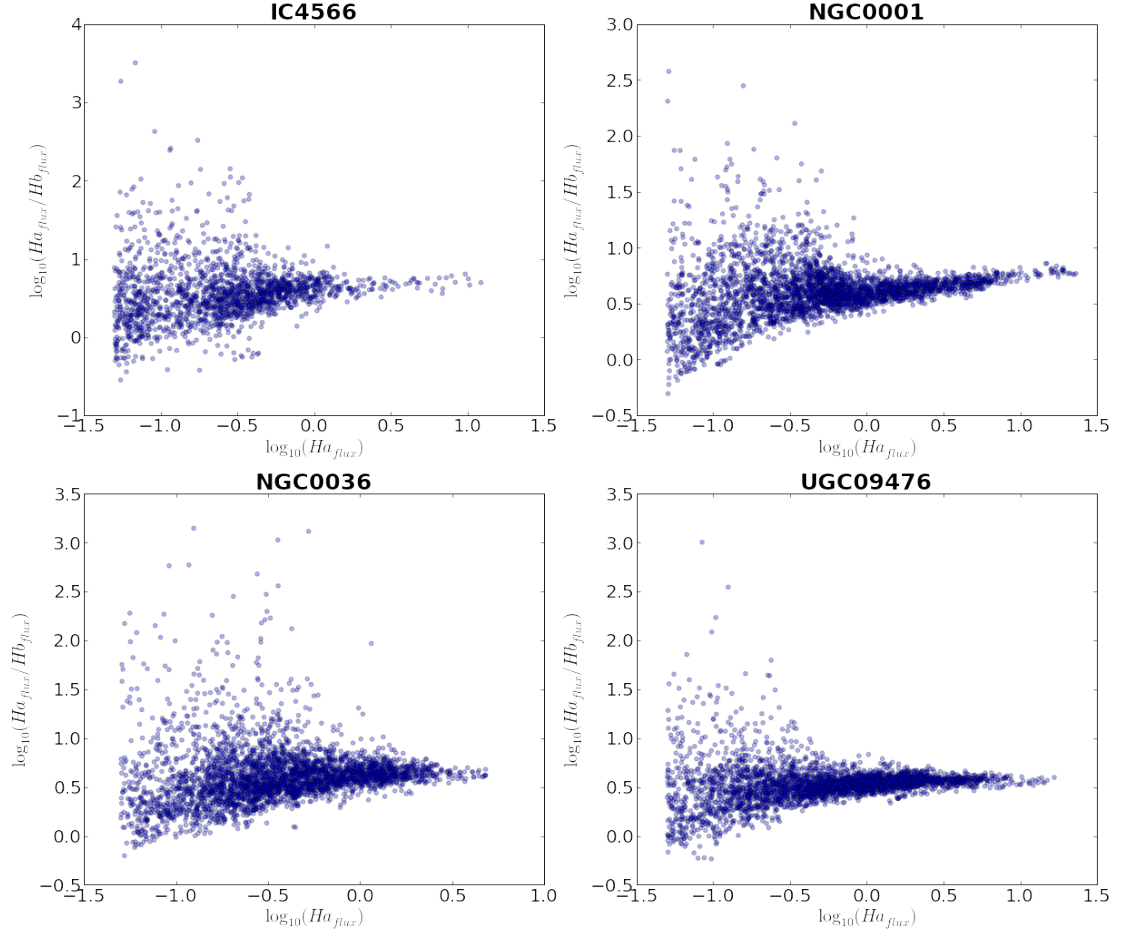


Figure 5.5: Distribution of $\log H_{\alpha}/H_{\beta}$ values for our representative galaxies graphed on the y axis. The H_{α} intensity (i.e. the SFR) is depicted on the x axis.

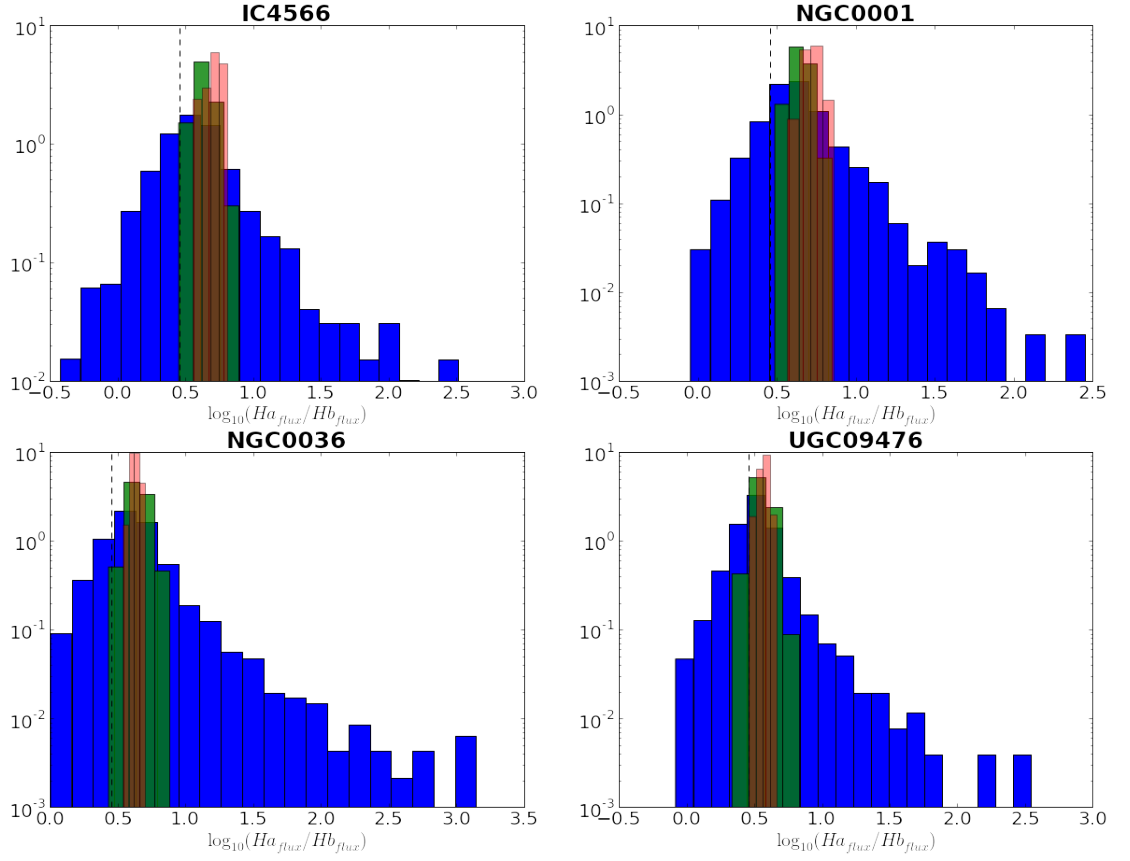


Figure 5.6: Distribution of $\log H\alpha/H\beta$ values for our representative galaxies plotted as histograms. The blue, green and red histograms correspond to the faint, mid range and bright regions of the $H\alpha$ spectra respectively. The segmented line lies on the theoretical value of the ratio.

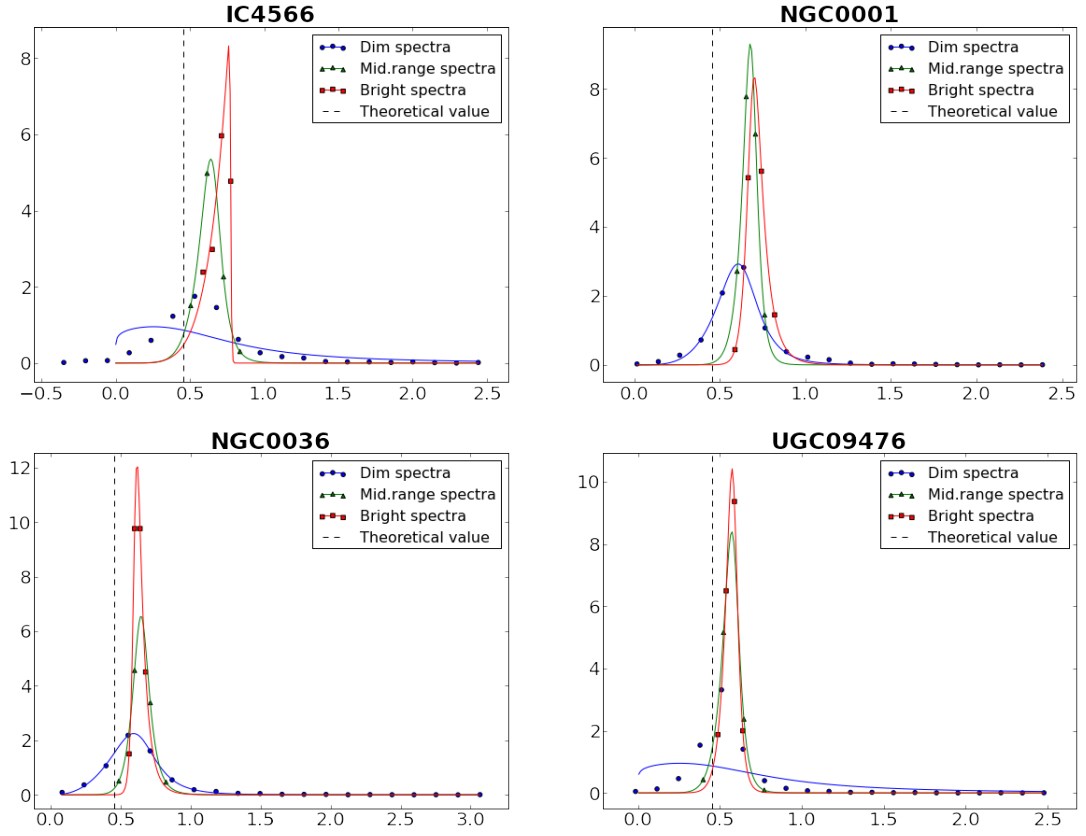


Figure 5.7: Distribution of H_α/H_β values, fitted as a double power law of the form shown in equation 2.2. The segmented line indicates the logarithm in base ten of the theoretical value of the H_α/H_β ratio.

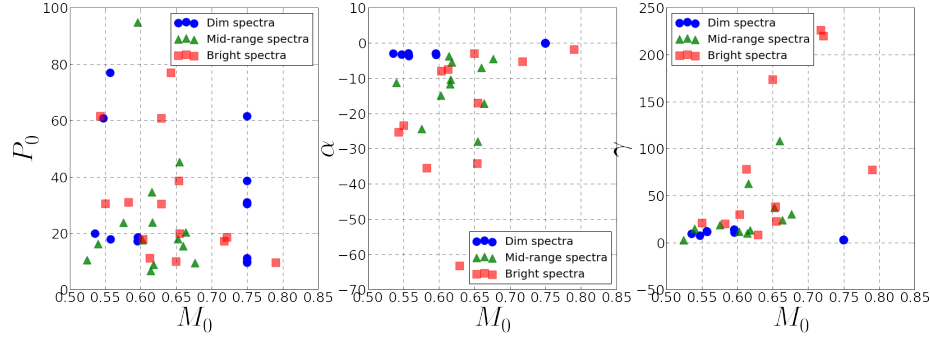


Figure 5.8: Comparison of M_0 and P_0 values

We also check the distribution for the OII EW. Once again, we separate our EW data into bright H_α , mid H_α and faint H_α . This separation of EW data follows the same criteria as the one performed on the H_α/H_β ratio. That means that this separation of data based in H_α intensity will allow us to separate regions of high SFR, lower SFR and lowest SFR in order to study the behavior of the OII EW and analyze if any SFR-dependent influences are detected.

A visualization of the OII EW maps is given in figure 5.9 along with a histogram of the data. Results for the representative galaxies are displayed in figure 5.10.

In order to have a clear understanding of the behavior of our data, we plot the values of the variance and kurtosis of the OII EW data. Once again separating the values in the three categories of H_α intensity, spanning the dim, the mid-range and the bright regions of the spectra.

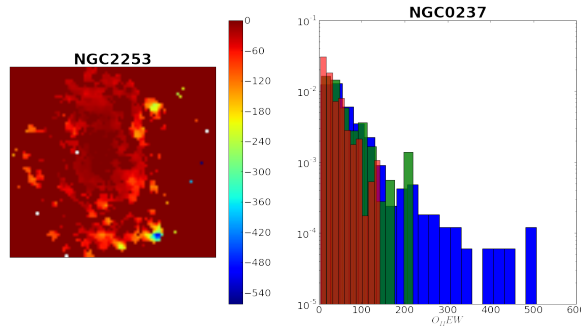


Figure 5.9: a) Map of the OII EW in NGC0237. b) A histogram showcasing the distribution of values for the OII EW

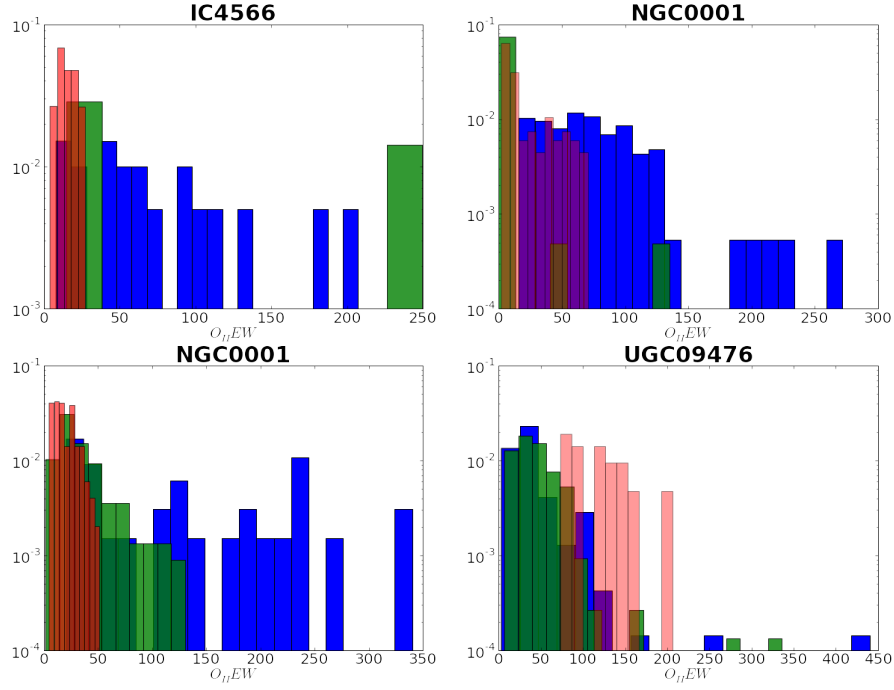


Figure 5.10: Distribution of the OII EW. The blue, green and red histograms correspond to the faint, mid and bright regions of the H_α spectra respectively.

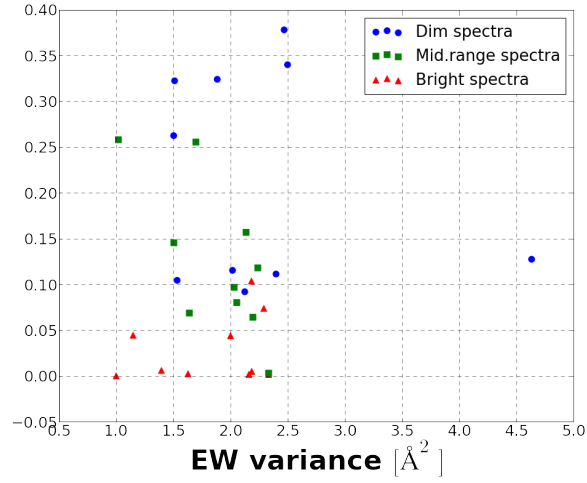


Figure 5.11: Variance versus kurtosis

Chapter 6

Discussion

6.1 The H_α/H_β ratio

According to [3], the H_α/H_β ratio fluctuates if stochasticity is present. Looking at the trimmed data in chapter four, figure 5.5, we can see that at a lower value of H_α , the H_α/H_β quotient starts becoming more disperse. This is consistent with the computational predictions since the H_α intensity is an indicator of star formation productivity, with higher H_α intensity corresponding to a higher SFR and a lower intensity to a lower SFR [8].

Once we visualize this distributions in figure 5.6, we can also recognize a distribution around the theoretical value of this ratio. In fact, the bright region of the H_α/H_β spectrum presents a more narrow distribution while the dimmer area presents a broader distribution.

In [2], Forero-Romero expands upon Fumagalli's [3] conclusions and proposes that this fluctuation should be present on other emission line ratios. We find looking at the histograms in figures 5.10 that distributions are also present in the OII EW. These distributions appear to behave in the same manner as the H_α/H_β ratio, with higher values presenting a lesser variation and lower values being more broadly scattered.

Even though we have found evidence of fluctuation of H_α/H_β and EW, we must be careful to consider this as evidence of stochasticity since interstellar reddening can cause similar effects. These reddening effects show that not all fluctuations of the H_α/H_β are due to stochasticity. Despite this, we can see from the histograms in figure 5.6 that this effect does not fully explain the distributions observed, as it only causes the values of the H_α/H_β ratio to move to the right. We can observe that in our histograms (figure 5.6) there are values of H_α/H_β that lie to the left of the theoretical value and are

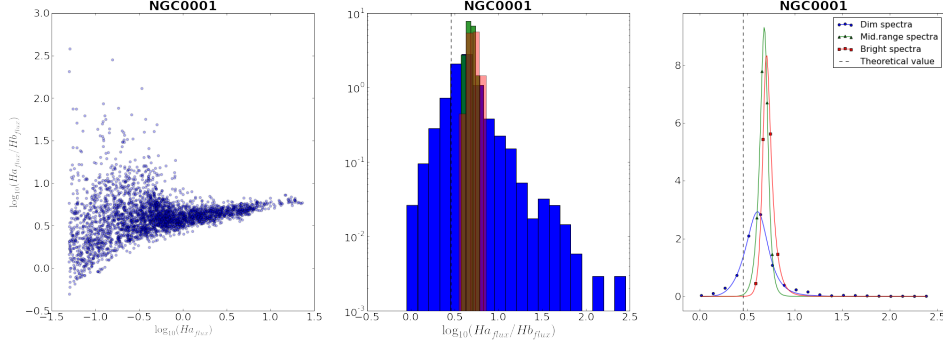


Figure 6.1: Results for NGC0001 including: a) Trimmed data of $\log H_\alpha$ vs. $\log H_\alpha/H_\beta$, b) Histogram of the data and c) Fitting of the probability distribution

not explained by this phenomenon. In particular, the majority of the data that lies to the left hand side of the theoretical value belongs to the H_α/H_β that belongs to the dim region of the H_α spectra. On the contrary, most of the mid-range and bright regions of the H_α spectra lie to the right of the theoretical value.

When analyzing the fitted curves for the histograms, we can see that at a higher SFR, the peaks become narrower and higher. This is also expected from the results found in [2]. In their results, the absence of stochasticity meant that the probability density function $P(\mathcal{M}|\text{SFR})$ presented in 2.2 would become a delta function centered around $\mathcal{M} = 1$.

This dispersion of values for the line ratio seems to be consistent with the theoretical prediction, but before drawing any conclusions we must treat the data to minimize external influences.

6.2 The OII EW

When analyzing the histograms in figure 5.10 we can observe that the histogram depicting the dim region of the spectra tends to be more broadly distributed than its more intense counterparts. The green bars indicating the regions of higher SFR are relatively more clustered the left side of the graph, and the bright region of the spectra presents the less distribution. This results seem to hint that stochasticity may be involved in the measured EW, but a correction for external effects must be performed.

Despite encouraging signs found in the OII EW, we also have the case of galaxies similar to UGC09476 presented in this work. Unfortunately, in some galaxies that were measured in the CALIFA survey there seems to be

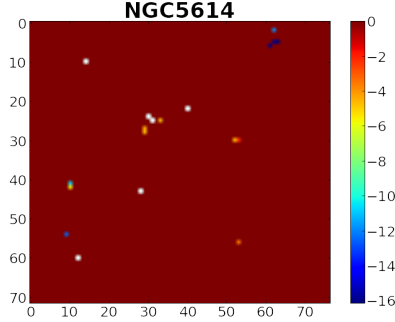


Figure 6.2: Bad OII EW data for galaxy NGC5614

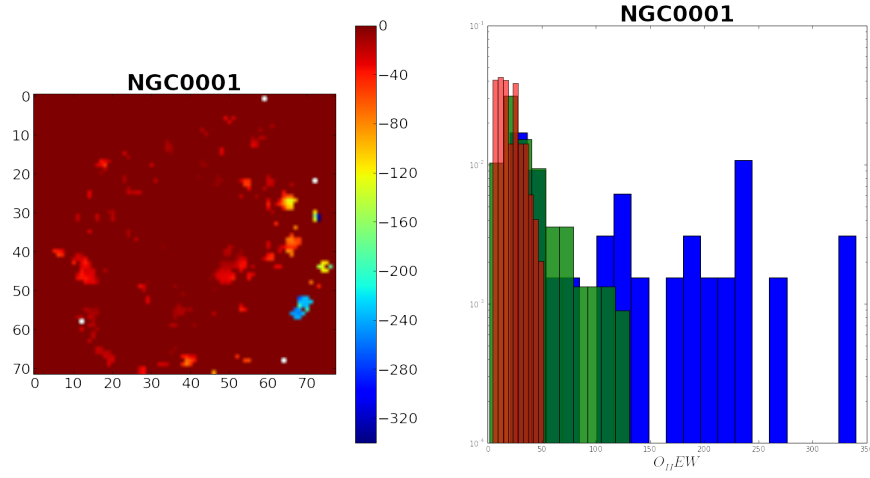


Figure 6.3: a) Map of the OII EW values in NGC0001. b) A histogram of the OII EW data

a great deal of bad pixels and seeing data of the nature of figure 6.2 was not uncommon. The data was not only scarce but it spanned only very few values of EW which generated poor quality histograms of the data.

Yet, a great deal of galaxies presented good data with which more work must be done in order to be able to name stochasticity as a candidate for the fluctuating effects of EW for multiple emission lines. For example, in the galaxy NGC0001 that we have presented in detail in this work, we can see in figure 6.3 that even though the data is not particularly abundant, the EW of OII covers a range of values sufficiently large to work with

Chapter 7

Conclusions

In this work we have set out to detect stochastic influence in the form of the fluctuation of several spectral parameters such the H_α/H_β ratio and the EW of the OII emission line. The method by which this was done was to discriminate between regions of high SFR and low SFR by way of that particular region's H_α intensity. Having identified these regions, we proceeded to illustrate the distributions of the values of the spectral parameters of interest to this work. Once we obtained these distributions, a fit was performed, following the results obtained in [2].

We have found that fluctuations of both the H_α/H_β ratio and EW of OII are indeed present in observational data.

Despite the influence of interstellar dust effects which were not accounted for in this work, we can say that the fluctuations detected are not fully explained by extinction effects. These extinction effects only produce fluctuation of parameters in one direction, that is, it causes the observed H_α/H_β ratio to take larger values than its theoretical value.

At first glance, it appears that stochasticity is a good candidate to explain the values of this H_α/H_β quotient that are measured to be of lesser value of the theoretical ratio although further work is required.

The fact that some fluctuation was also detected on the OII EW may also indicate that, as presented in [2], fluctuation of spectral quantities is also found in other emission line ratios, despite [2] and [3] focusing on the Ly_α EW and the H_α/H_β ratio.

A successful characterization of the behavior of the distribution of values of H_α/H_β was obtained based on the computational predictions published in [2], including the fact that this distribution appears to be dependent on the SFR as predictions stated.

7.1 Further work

Further work on the theoretical behavior of the distribution of EW at different SFRs is needed. Expanding on the conclusions derived in [2] we can more reliably quantify the effects of stochasticity.

In order to more be able to suggest stochasticity as a significant influence in regions of low SFR we must perform a correction for dust on our data. Applying this correction will allow us to analyze our results with minimal interference from external sources. To do this we must use an extinction map in order to quantify the influence of interstellar reddening and then perform our analysis on the treated data and determine if stochasticity is observed.

The fitting procedure returned the initial guesses of the free parameters on several occasions, which indicates the necessity to obtain a more educated guess for the first iteration of this procedure. Initial guesses were taken from computational results presented in [2], though that work focused solely on the Ly_α emission line.

A more in depth analysis of the OII EW must be done, although it will not include the same number of galaxies as the H_α/H_β ratio since some data is missing or is not suitable for performing any analysis. Moreover, a more detailed description of the behavior of the OII EW dispersion is required.

Chapter 8

Appendix

8.1 List of galaxies

Name			
UGC00005	NGC2880	UGC09067	NGC6478
NGC7819	NGC2906	NGC5520	NGC6497
IC1528	NGC2916	NGC5614	UGC11262
UGC00036	UGC05108	NGC5630	NGC6941
NGC0001	UGC05358	NGC5720	NGC6978
NGC0036	UGC05359	UGC09476	UGC11649
UGC00312	NGC3106	NGC5784	NGC7311
NGC0171	NGC3994	NGC5888	NGC7321
NGC0180	NGC4003	NGC5930	UGC12127
NGC0192	UGC07012	IC4566	UGC12185
NGC0237	NGC4185	NGC6004	UGC12224
NGC0477	NGC4210	NGC6020	NGC7549
IC1683	IC0776	NGC6021	NGC7563
NGC0496	NGC4470	NGC6032	NGC7562
NGC0774	UGC08107	NGC6063	NGC7625
NGC0776	UGC08231	IC1199	NGC7631
NGC1349	UGC08234	NGC6125	NGC7653
NGC1645	NGC5000	NGC6132	NGC7716
UGC03253	NGC5205	NGC6146	NGC7738
NGC2253	NGC5216	NGC6154	UGC12816
NGC2347	UGC08733	NGC6173	NGC7489
UGC03995	UGC08781	UGC10693	UGC12864
NGC2449	NGC5378	UGC10695	NGC7800
NGC2730	NGC5406	IC1256	NGC5947

8.2 Additional results

	P_0	\mathcal{M}_0	α	γ
IC4566	1.15	0.75	-0.13	2.67
	9.97257057	0.66439036	-6.90804198	15.11022712
	9.31448729	0.77507363	-5.63906206	246.58977299
NGC0001	5.45274152	0.646262	-3.93214833	8.60231608
	17.90378157	0.68880842	-13.79614347	24.71101529
	16.38690053	0.69380378	-21.93405233	14.44680814
NGC0036	3.99989437	0.66192434	-2.48524458	6.9536647
	13.02396505	0.65278304	-11.16069931	14.25713254
	22.28399342	0.60634967	-34.49879557	14.1615634
UGC09476	1.15	0.75	-0.13	2.67
	15.85363576	0.5869998	-9.32051303	18.96592234
	19.79426654	0.58477093	-12.99367006	25.14352254
NGC0237	6.07363614	0.53588776	-3.0693835	9.23165432
	9.35964361	0.67672432	-4.6064685	30.05004698
	19.82078282	0.65515464	-17.09466414	22.49513438
NGC4210	6.70203691	0.55783254	-3.768397	11.30558088
	16.11252471	0.54029705	-11.34576718	14.55231085
	17.79401005	0.60358477	-8.06582396	29.69265484
UGC09067	1.15	0.75	-0.13	2.67
	20.2522966	0.66382498	-17.26512941	23.71938356
	38.51961161	0.65405959	-34.25595988	38.05965643
NGC0776	1.15	0.75	-0.13	2.67
	17.86224451	0.65272885	-10.2694177	36.92624162
	3.03273802e+01	6.29415698e-01	-1.47235683e+03	8.03508911
NGC4185	1.15	0.75	-0.13	2.67
	34.5082516	0.6160257	-11.76223282	62.5459429
	30.40804093	0.55054484	-23.51395979	20.75471106
NGC6941	1.15	0.75	-0.13	2.67
	8.74168013	0.61839248	-5.56878649	12.97466935
	11.08774536	0.61310135	-7.5913821	77.92311115
NGC5947	6.07516876	0.55725356	-3.01677251	11.99239462
	9.46958792e+01	5.96046441e-01	-1.02651949e+03	5.06593218e+01
	7.68500907e+01	6.42779504e-01	-1.67143389e+01	2.78970188e+03

	P_0	\mathcal{M}_0	α	γ
NGC5630	1.15	0.75	-0.13	2.67
	23.76983133	0.61678668	-10.47539771	177.59963355
	6.14432635e+01	5.43391105e-01	-2.53863573e+01	7.07883254e+02
NGC7819	5.64575733	0.54766878	-3.34628371	7.26733786
	45.17486167	0.65490677	-28.02002097	478.42703003
	60.70074969	0.62928871	-63.29956548	40.69369206
IC0776	6.31978756	0.45989236	-2.96673728	6.77244842
	11.28915937	0.66260033	-1.71239986	172.28450106
	1.79592765	1.60730694	1.98527051	59.03888205
NGC0171	1.15	0.75	-0.13	2.67
	15.3519312	0.66004673	-7.11830138	107.9808245
	9.91740148	0.65004505	-3.05285332	173.32019704
NGC5520	5.77666534	0.59580223	-3.03887638	13.71760963
	17.47499974	0.60290305	-14.96342177	11.45619764
	17.10882	0.71787408	-5.3603214	225.82113638
NGC5378	1.15	0.75	-0.13	2.67
	6.59069134	0.6144234	-3.82666631	9.64549458
	9.5075563	0.79044972	-1.91515454	77.19950244
NGC3614	5.88905924	0.59618067	-3.4349813	10.56069665
	10.41387827	0.52476607	-249.25800168	2.39283009
	18.48493963	0.72161139	-2.8612163	219.65672529
NGC5406	4.81161509	0.6245487	-2.67347417	9.5757696
	0.61242192	0.74335932	15.11232105	33.26679814
	16.76435234	0.65746016	-8.24985774	87.51968968
NGC2347	1.15	0.75	-0.13	2.67
	23.68235267	0.57598245	-24.45526185	18.52368243
	30.90784931	0.5830965	-35.559818	19.7851584

Bibliography

- [1] C. J. Lada and E. A. Lada. “Embedded Clusters in Molecular Clouds”. In: 41 (2003), pp. 57–115. DOI: 10.1146/annurev.astro.41.011802.094844. eprint: astro-ph/0301540.
- [2] J. E. Forero-Romero and M. Dijkstra. “Effects of star-formation stochasticity on the Ly α and Lyman continuum emission from dwarf galaxies during reionization”. In: 428 (Jan. 2013), pp. 2163–2170. DOI: 10.1093/mnras/sts177. arXiv: 1206.0726.
- [3] M. Fumagalli, R. L. da Silva, and M. R. Krumholz. “Stochastic Star Formation and a (Nearly) Uniform Stellar Initial Mass Function”. In: 741, L26 (Nov. 2011), p. L26. DOI: 10.1088/2041-8205/741/2/L26. arXiv: 1105.6101.
- [4] L. Mas-Ribas, M. Dijkstra, and J. E. Forero-Romero. “Boosting Ly α and HeII 1640Å Line Fluxes from Pop III Galaxies: Stochastic IMF Sampling and Departures from Case-B”. In: *ArXiv e-prints* (Sept. 2016). arXiv: 1609.02150.
- [5] S. F. Sánchez et al. “CALIFA, the Calar Alto Legacy Integral Field Area survey. I. Survey presentation”. In: 538, A8 (Feb. 2012), A8. DOI: 10.1051/0004-6361/201117353. arXiv: 1111.0962.
- [6] J. Sánchez Almeida et al. “Qualitative Interpretation of Galaxy Spectra”. In: 756, 163 (Sept. 2012), p. 163. DOI: 10.1088/0004-637X/756/2/163. arXiv: 1207.3928.
- [7] S. F. Sánchez et al. “Pipe3D, a pipeline to analyze Integral Field Spectroscopy Data: II. Analysis sequence and CALIFA dataproducts”. In: 52 (Apr. 2016), pp. 171–220. arXiv: 1602.01830 [astro-ph.IM].
- [8] L. J. Kewley et al. “The H α and Infrared Star Formation Rates for the Nearby Field Galaxy Survey”. In: 124 (Dec. 2002), pp. 3135–3143. DOI: 10.1086/344487. eprint: astro-ph/0208508.

- [9] R. C. Kennicutt Jr. “Star Formation in Galaxies Along the Hubble Sequence”. In: 36 (1998), pp. 189–232. DOI: 10.1146/annurev.astro.36.1.189. eprint: astro-ph/9807187.
- [10] JE Andrews et al. “AN INITIAL MASS FUNCTION STUDY OF THE DWARF STARBURST GALAXY NGC 4214Based on observations made with the NASA/ESA Hubble Space Telescope, obtained at the Space Telescope Science Institute, which is operated by the Association of Universities for Research in Astronomy, Inc., under NASA contract NAS 5-26555. These observations are associated with program GO-11360.” In: *The Astrophysical Journal* 767.1 (2013), p. 51.
- [11] R. L. da Silva, M. Fumagalli, and M. R. Krumholz. “SLUG - Stochastically Lighting Up Galaxies - II. Quantifying the effects of stochasticity on star formation rate indicators”. In: 444 (Nov. 2014), pp. 3275–3287. DOI: 10.1093/mnras/stu1688. arXiv: 1403.4605.
- [12] Robert L. da Silva, Michele Fumagalli, and Mark Krumholz. “SLUGStochastically Lighting Up Galaxies. I. Methods and Validating Tests”. In: *The Astrophysical Journal* 745.2 (2012), p. 145. URL: <http://stacks.iop.org/0004-637X/745/i=2/a=145>.
- [13] A. Domnguez et al. “Dust Extinction from Balmer Decrements of Star-forming Galaxies at $0.75 < z < 1.5$ with Hubble Space Telescope/Wide-Field-Camera 3 Spectroscopy from the WFC3 Infrared Spectroscopic Parallel Survey”. In: *The Astrophysical Journal* 763.2 (2013), p. 145. URL: <http://stacks.iop.org/0004-637X/763/i=2/a=145>.
- [14] M. Geha et al. “The Stellar Initial Mass Function of Ultra-faint Dwarf Galaxies: Evidence for IMF Variations with Galactic Environment”. In: 771, 29 (July 2013), p. 29. DOI: 10.1088/0004-637X/771/1/29. arXiv: 1304.7769.
- [15] E. E. Salpeter. “The Luminosity Function and Stellar Evolution.” In: 121 (Jan. 1955), p. 161. DOI: 10.1086/145971.